A Novel Strong-Coupling Pseudo-Spectral Method for Numerical Studies of Two-Layer Turbulent Channel Flows

Tong Wu[1,2], Zixuan Yang[1,3,*], Shizhao Wang[1,3] and Guowei He[1,3]

[1] *State Key Laboratory of Nonlinear Mechanics, Institute of Mechanics, Chinese Academy of Sciences, China.*
[2] *Laboratoire de Mécanique Physique, École Centrale de Pékin, Beihang University, China.*
[3] *School of Engineering Sciences, University of Chinese Academy of Sciences, China.*

Abstract. A new method is proposed to simulate a coupled air-water two-layer turbulent channel flow. A numerically effective dynamic viscosity is implemented to calculate the viscous momentum flux at the interface, leading to a strong-coupling scheme for the evolution of air and water motions. The direct numerical simulation results are compared with those in the literature obtained from a weak-coupling scheme. It is discovered that while the turbulence statistics of the air phase based on the strong- and weak-coupling schemes are close to each other, the results on the water side are influenced by the coupling approach, especially near the water surface.

1 Introduction

The investigations of air-water interactions are foundations of many applications in ocean science, environmental engineering, and chemical engineering. The computational fluid dynamics (CFD) are used broadly for studying these problems. During the last two decades, various physical models of air-water interactions have been studied through CFD based on different numerical schemes.

CFD studies of air-water interface can be categorized into one-fluid and two-fluid simulations. In the one-fluid simulation, the governing equations of only one fluid phase

---

are solved, while the effect of the other phase is modeled through appropriate boundary conditions. Specifically, in the numerical studies of air flows over a water surface, the water surface is usually treated as a flat or wavy boundary with prescribed surface roughness and velocity [1–4], while in a large number of simulations of water flows, the effect of air is imposed through a given shear stress at the water surface [5–9]. The one-fluid simulation is usually conducted to study physical problems without strong two-way interactions between the two fluid phases.

In the two-fluid simulation, it is challenging and expensive to track or capture the deformation of the interface between two fluid phases [10–12]. A simplified physical model for two-fluid simulation is a two-layer channel flow [13,14], which has been studied for fundamental research of turbulent motions in the vicinity of the interface. In the two-layer channel flow, the interface between two fluid phases is assumed to be flat [14], corresponding to flow conditions with large gravity or large surface tension. The two-layer channel flow features a simple interface geometry, which makes it possible to solve the motions of two fluid phases by using a pseudo-spectral scheme [15]. The high accuracy and high efficiency of the pseudo-spectral method are desired features of numerical algorithms [16–19].

While the numerical method for simulating one-layer channel flow is mature, the key of the numerical method for simulating two-layer channel flow is the implementation of the interface condition. Lombardi *et al.* [13] proposed a staggered advancement method. In the first-half timestep of this method, the velocity at the water surface is used as the boundary condition of the air flow, while in the second-half timestep, the shear stress at the air bottom is used as a momentum source to drive the water motion. This method is known as a weak-coupling approach as the continuities in velocity and stress are not satisfied simultaneously.

To develop a strong-coupling method, the use of inner iteration is an option [14, 20]. However, this method significantly increases the computational cost. Based on the literature reviewed above, we have developed a strong-coupling method for two-layer turbulent channel flow by implementing an effective viscosity at the interface, such that the motions of two fluid phases are evolved synchronically without applying any inner iteration. The proposed method is then tested in the context of a low-Reynolds-number two-layer turbulent Couette flow. The turbulent statistics are compared with the results based on the weak-coupling method of Liu *et al.* [14]. The remainder of this paper is organized as follows. In Section 2, the numerical methods are introduced. Then, the results are presented and discussed in Section 3, followed by the conclusions in Section 4.

2 Numerical method

2.1 Computational domain and governing equations

Fig. 1 shows the computational domain of a two-layer channel flow. As shown, x_1, x_2, and x_3 represent the streamwise, spanwise, and vertical directions, respectively. The air-
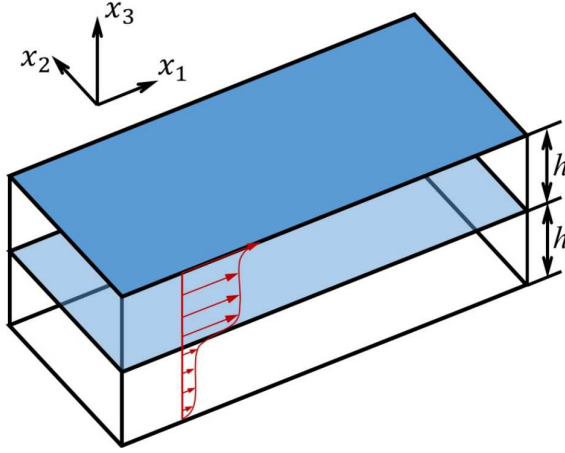
Figure 1: Computational domain and coordinate system for two-layer turbulent channel flow.

water interface is set to $x_3 = 0$. The bottom of water and the top of air are located at $x_3 = -h$ and $x_3 = h$, respectively. The two-layer channel flow is governed by the following continuity and momentum equations:

$$\frac{\partial u_i}{\partial x_i} = 0, \tag{2.1}$$

$$\frac{\partial u_i}{\partial t} + \frac{\partial (u_i u_j)}{\partial x_j} = -\frac{1}{\rho}\frac{\partial p}{\partial x_i} + \frac{1}{\rho}\frac{\partial}{\partial x_j}(2\mu S_{ij}), \tag{2.2}$$

where t represents the time; u_1, u_2, and u_3 denote the velocity components in the x_1-, x_2-, and x_3-directions, respectively; p is the pressure; $\rho = \rho(x_3)$ and $\mu = \mu(x_3)$ are density and dynamic viscosity, varying with the fluid phases; and $S_{ij} = (u_{i,j} + u_{j,i})/2$ is the strain-rate tensor. Because the values of ρ and μ are independent of x_1 and x_2, the momentum equation can be rewritten as

$$\frac{\partial u_i}{\partial t} + \frac{\partial (u_i u_j)}{\partial x_j} = -\frac{1}{\rho}\frac{\partial p}{\partial x_i} + \frac{1}{\rho}\frac{\partial}{\partial x_j}\left(\mu\frac{\partial u_i}{\partial x_j}\right) + \frac{1}{\rho}\frac{\partial \mu}{\partial x_3}\frac{\partial u_3}{\partial x_i}. \tag{2.3}$$

Considering that the value of $\partial \mu/\partial x_3$ in Eq. (2.3) is zero except for the interface, while the velocity at the interface is determined by the interface condition, the last term in Eq. (2.3) can be omitted in the simulation. As a result, the momentum equation can be further simplified to

$$\frac{\partial u_i}{\partial t} + \frac{\partial (u_i u_j)}{\partial x_j} = -\frac{1}{\rho}\frac{\partial p}{\partial x_i} + \frac{1}{\rho}\frac{\partial}{\partial x_j}\left(\mu\frac{\partial u_i}{\partial x_j}\right). \tag{2.4}$$

At the interface, the horizontal velocity is continuous, while the vertical velocity is fixed to zero to keep the interface static [14], viz.

$$u_{1a} = u_{1w}, \quad u_{2a} = u_{2w}, \quad u_{3a} = u_{3w} = 0, \tag{2.5}$$

where subscripts a and w represent air and water, respectively. Furthermore, the continuity in shear stress is also applied at the air-water interface, expressed as [14]

$$\mu_a \frac{\partial u_{1a}}{\partial x_3} = \mu_w \frac{\partial u_{1w}}{\partial x_3}, \quad \mu_a \frac{\partial u_{2a}}{\partial x_3} = \mu_w \frac{\partial u_{2w}}{\partial x_3}. \tag{2.6}$$

At the water bottom, a no-slip condition is prescribed as

$$u_1(x_3 = -h) = u_2(x_3 = -h) = u_3(x_3 = -h) = 0. \tag{2.7}$$

At the top of the computational domain, the air is driven by a constant shear stress τ_{top} in the streamwise direction, while vertical velocity and spanwise shear stress are set to zero. The boundary condition at the top is expressed as [14]

$$\tau_{\text{top}} = \mu_a \frac{\partial u_1(x_3 = h)}{\partial x_3} = const., \quad \frac{\partial u_2(x_3 = h)}{\partial x_3} = 0, \quad u_3(x_3 = h) = 0. \tag{2.8}$$

2.2 Time advancement of the velocity field

A Crack-Nicolson scheme is used for the viscous term, while a second-order Adam-Bashforth scheme is used for the convection term. The temporally discretized form of the momentum equation is expressed as [21,22]

$$\frac{v_i - u_i^{(n)}}{\Delta t} = \frac{3R_i^{(n)} - R_i^{(n-1)}}{2} + \frac{1}{\rho} \frac{\partial}{\partial x_j} \left[\mu \frac{\partial}{\partial x_j} \left(\frac{v_i + u_i^{(n)}}{2} \right) \right], \tag{2.9}$$

where superscript (n) denotes the velocity field at time step n; v_i is the velocity at an intermediate step; and $R_i = -\partial(u_i u_j)/\partial x_j$ is the convection term in the momentum equation. In order to solve v_i, Eq. (2.9) is rewritten as [21,22]

$$\frac{2v_i}{\Delta t} - \frac{1}{\rho} \frac{\partial}{\partial x_j} \left(\mu \frac{\partial v_i}{\partial x_j} \right) = \frac{2u_i^{(n)}}{\Delta t} + 3R_i^{(n)} - R_i^{(n-1)} + \frac{1}{\rho} \frac{\partial}{\partial x_j} \left(\mu \frac{\partial u_i^{(n)}}{\partial x_j} \right). \tag{2.10}$$

The intermediate velocity field v_i is then projected to satisfy the divergence-free condition given by Eq. (2.1). The projection step is expressed as [23]

$$\frac{u_i^{(n+1)} - v_i}{\Delta t} = -\frac{1}{\rho} \frac{\partial \Pi^{(n+1)}}{\partial x_i}, \tag{2.11}$$

where Π is a pseudo pressure, which is related to the pressure p as $p^{(n+1/2)} = \Pi^{(n+1)} - \Delta t \nabla \cdot (\mu \nabla \Pi^{(n+1)})/2$. Taking the divergence of Eq. (2.11) and applying the divergence-free condition, the Poisson equation of Π is given as [23]

$$\frac{\partial}{\partial x_i} \left(\frac{1}{\rho} \frac{\partial \Pi^{(n+1)}}{\partial x_i} \right) = \frac{1}{\Delta t} \frac{\partial v_i}{\partial x_i}. \tag{2.12}$$

2.3 Spatial discretization

The hybrid pseudo-spectral and finite-difference method is used for spatial discretization. The pseudo-spectral method features a high accuracy and a high computational efficiency, which is usually used in flows with simple geometries. The present code is developed by modifying the pseudo-spectral method code developed in Xu's group, which has been well validated in many applications [24–30]. The detailed scheme for spatial discretization is described below.

An arbitrary field variable $\phi(x_1, x_2, x_3, t)$ is expanded into Fourier series in the streamwise and spanwise directions as [15]

$$\phi(x_1, x_2, x_3, t) = \sum_{n_1=-N_1/2}^{N_1/2-1} \sum_{n_2=-N_2/2}^{N_2/2-1} \hat{\phi}(n_1, n_2, x_3, t) e^{i(n_1 k_{01} x_1 + n_2 k_{02} x_2)}, \tag{2.13}$$

where $i = \sqrt{-1}$ is the imaginary unit; $n_1 \in [-N_1/2, N_1/2-1]$ and $n_2 \in [-N_2/2, N_2/2-1]$ are two integers; N_1 and N_2 are the total resolved wavenumbers in the x_1- and x_2-directions, respectively; $k_{01} = 2\pi/L_1$ and $k_{02} = 2\pi/L_2$ are the lowest positive wavenumbers in the x_1- and x_2-directions, respectively, with L_1 and L_2 being the computational domain sizes in the corresponding directions (Fig. 1). In the spectral space, the streamwise and spanwise derivatives of ϕ are calculated by multiplying $i n_1 k_{01}$ and $i n_2 k_{02}$ to $\hat{\phi}$, respectively. Eqs. (2.10)-(2.12) are then rewritten as

$$\left[\frac{2}{\Delta t} - \frac{i(n_1^2 k_{01}^2 + n_2^2 k_{02}^2)\mu}{\rho} \right] \hat{v}_i - \frac{1}{\rho} \frac{\partial}{\partial x_3} \left(\mu \frac{\partial \hat{v}_i}{\partial x_3} \right)$$
$$= 3\hat{R}_i^{(n)} - \hat{R}_i^{(n-1)} + \left[\frac{2}{\Delta t} - \frac{i(n_1^2 k_{01}^2 + n_2^2 k_{02}^2)\mu}{\rho} \right] \hat{u}_i^{(n)} - \frac{1}{\rho} \frac{\partial}{\partial x_3} \left(\mu \frac{\partial \hat{u}_i^{(n)}}{\partial x_3} \right), \tag{2.14}$$

$$\frac{\hat{u}_i^{(n+1)} - \hat{v}_i}{\Delta t} = -\frac{1}{\rho} \left(i n_1 k_{01} \hat{\Pi}^{(n+1)} \delta_{i1} + i n_2 k_{02} \hat{\Pi}^{(n+1)} \delta_{i2} + \frac{\partial \hat{\Pi}^{(n+1)}}{\partial x_3} \delta_{i3} \right), \tag{2.15}$$

$$-\frac{n_1^2 k_{01}^2 + n_2^2 k_{02}^2}{\rho} \hat{\Pi}^{(n+1)} + \frac{\partial}{\partial x_3} \left(\frac{1}{\rho} \frac{\partial \hat{\Pi}^{(n+1)}}{\partial x_3} \right) = \frac{1}{\Delta t} \left(i n_1 k_{01} v_1 + i n_2 k_{02} v_2 + \frac{\partial v_3}{\partial x_3} \right), \tag{2.16}$$

where δ_{ij} is the Kronecker Delta. The term $\hat{R}_i$ in Eq. (2.14) is defined as

$$\hat{R}_i = -i(n_1 k_{01} \widehat{u_i u_1} + n_2 k_{02} \widehat{u_i u_2}) - \frac{\partial \widehat{u_i u_3}}{\partial x_3}, \tag{2.17}$$

where $\widehat{u_i u_j}$ is the Fourier coefficients of $u_i u_j$, which is calculated in the physical space. The 3/2 rule is applied to eliminate the aliasing error [15].

In the vertical direction, staggered grids are used. The grid points are located at

$$
x_{3,k} =
\begin{cases}
\dfrac{1}{2}\left\{ \beta^{-1}\tanh\left[\left(\dfrac{4k}{N_3}-1\right)\tanh^{-1}\beta\right]-1\right\}, & k=0,1,\cdots,\dfrac{N_3}{2}, \\[4mm]
\dfrac{1}{2}\left\{ \beta^{-1}\tanh\left[\left(\dfrac{4k}{N_3}-3\right)\tanh^{-1}\beta\right]+1\right\}, & k=\dfrac{N_3}{2},\dfrac{N_3}{2}+1,\cdots,N_3,
\end{cases}
\tag{2.18}
$$

where the value of the coefficient β is set to 0.985. The vertical velocity u_3 is defined at the grid points, while u_1, u_2, and Π are defined at grid centers, located at $x_{3,k+1/2} = (x_{3,k}+x_{3,k+1})/2$. The vertical derivative $\partial/\partial x_3$ is calculated using a central difference scheme. In Eq. (2.17), $\partial(u_i u_3)/\partial x_3$ are collocated with u_i in the vertical direction. The values of $\partial(u_i u_3)/\partial x_3$ are calculated as

$$
\begin{cases}
\left(\dfrac{\partial\widehat{u_i u_3}}{\partial x_3}\right)_{k+1/2} = \dfrac{(\widehat{u_i u_3})_{k+1}-(\widehat{u_i u_3})_{k}}{x_{3,k+1}-x_{3,k}}, & i=1,2, \\[4mm]
\left(\dfrac{\partial\widehat{u_i u_3}}{\partial x_3}\right)_{k} = \dfrac{(\widehat{u_i u_3})_{k+1/2}-(\widehat{u_i u_3})_{k-1/2}}{x_{3,k+1/2}-x_{3,k-1/2}}, & i=3,
\end{cases}
\tag{2.19}
$$

where $u_{1,k}$, $u_{2,k}$, and $u_{3,k+1/2}$ are calculated using a linear interpolation. Note that at the interface, $u_{i,I}u_{3,I}=0$ holds strictly due to the condition $u_{3,I}=0$, where $I=N_3/2$ is the index of the interface. Therefore, the values of $u_{1,I}$ and $u_{2,I}$ do not influence the simulation results, such that no special treatment is needed for calculating $u_{1,I}$ and $u_{2,I}$ to satisfy the interface conditions.

Nevertheless, the interface conditions need to be considered in the calculation of the viscous terms. In Eq. (2.14) the viscous terms with the vertical derivative are discretized as

$$
\begin{cases}
\left[\dfrac{1}{\rho}\dfrac{\partial}{\partial x_3}\left(\mu\dfrac{\partial\hat{v}_i}{\partial x_3}\right)\right]_{k+1/2} = \dfrac{1}{\rho_{k+1/2}}\dfrac{\mu_{k+1}\frac{(\hat{v}_i)_{k+3/2}-(\hat{v}_i)_{k+1/2}}{x_{3,k+3/2}-x_{3,k+1/2}}-\mu_k\frac{(\hat{v}_i)_{k+1/2}-(\hat{v}_i)_{k-1/2}}{x_{3,k+1/2}-x_{3,k-1/2}}}{x_{3,k+1}-x_{3,k}}, & i=1,2, \\[5mm]
\left[\dfrac{1}{\rho}\dfrac{\partial}{\partial x_3}\left(\mu\dfrac{\partial\hat{v}_i}{\partial x_3}\right)\right]_{k} = \dfrac{1}{\rho_k}\dfrac{\mu_{k+1/2}\frac{(\hat{v}_i)_{k+1}-(\hat{v}_i)_{k}}{x_{3,k+1}-x_{3,k}}-\mu_{k-1/2}\frac{(\hat{v}_i)_{k}-(\hat{v}_i)_{k-1}}{x_{3,k}-x_{3,k-1}}}{x_{3,k+1/2}-x_{3,k-1/2}}, & i=3.
\end{cases}
\tag{2.20}
$$

The viscous term on the right-hand side of Eq. (2.14) is discretized using the same scheme by replacing $\hat{v}_i$ with $\hat{u}_i^{(n)}$. Substituting Eq. (2.20) into Eq. (2.14) results in a tridiagonal linear equation system of $\hat{v}_i$. In the linear equations of $\hat{v}_1$ and $\hat{v}_2$, the value of μ_I is needed, which is determined using the interface condition. According to Eqs. (2.5) and (2.6), the streamwise shear stress at the interface can be approximated as

$$
\mu\frac{\partial u_1}{\partial x_3} = \mu_w\frac{u_I-u_{I-1/2}}{x_{3,I}-x_{3,I-1/2}} = \mu_a\frac{u_{I+1/2}-u_I}{x_{3,I+1/2}-x_{3,I}} = \mu_I\frac{u_{I+1/2}-u_{I-1/2}}{x_{3,I+1/2}-x_{3,I-1/2}}.
\tag{2.21}
$$

Because the grid is symmetric about the interface (see Eq. 2.18), $x_{3,I}-x_{3,I-1/2}=x_{3,I+1/2}-x_{3,I}=(x_{3,I+1/2}-x_{3,I-1/2})/2$ holds. Eq. (2.21) can be then simplified to

$$
\mu_w(u_I-u_{I-1/2}) = \mu_a(u_{I+1/2}-u_I) = \mu_I\frac{u_{I+1/2}-u_{I-1/2}}{2},
\tag{2.22}
$$

from which it can be derived that μ_I is the harmonic averaging of μ_a and μ_w:

$$\mu_I = \frac{2\mu_a\mu_w}{\mu_a + \mu_w}. \tag{2.23}$$

Although Eq. (2.23) is derived based on the continuity of the streamwise shear stress at the interface, the expression of μ_I obtained from the continuity of the spanwise shear stress takes the same form. Equation (2.23) holds strictly at an arbitrary time instant and an arbitrary location at the interface. As a result, the effective viscosity μ_I can be used to calculate the viscous shear stress at the interface in the spectral space. Furthermore, no approximation is involved in the derivation from Eq. (2.21) to (2.23). This indicates that through the use of the effective viscosity, the motions of air and water are strongly coupled, with their governing equations evolved synchronically.

After evolving the velocity field from $u_i^{(n)}$ to the intermediate field v_i, Eq. (2.16) is solved to obtain the pseudo pressure $\Pi^{(n+1)}$. The term including the vertical derivative on the left-hand side of Eq. (2.16) is approximated as

$$\left[\frac{\partial}{\partial x_3}\left(\frac{1}{\rho}\frac{\partial\hat{\Pi}}{\partial x_3}\right)\right]_{k+1/2} = \frac{\frac{1}{\rho_{k+1}}\frac{\hat{\Pi}_{k+3/2}-\hat{\Pi}_{k+1/2}}{x_{3,k+3/2}-x_{3,k+1/2}} - \frac{1}{\rho_k}\frac{\hat{\Pi}_{k+1/2}-\hat{\Pi}_{k-1/2}}{x_{3,k+1/2}-x_{3,k-1/2}}}{x_{3,k+1}-x_{3,k}}. \tag{2.24}$$

This equation is only used to discretize the Poisson equation of $\hat{\Pi}$ at inner grid points (for $k=1,\cdots,I-2, I+1,\cdots,N_3-2$), while the discretizations near the boundary and interface (for $k=0$, $I-1$, I, and N_3-1) need modifications. In the proposed method, both $\hat{u}_3^{(n+1)}=0$ and $\hat{v}_3=0$ are imposed to satisfy the impermeable condition at the interface and boundary given by Eqs. (2.5), (2.7) and (2.8). Therefore, the condition $\partial\hat{\Pi}/\partial x_3=0$ holds according to Eq. (2.15). Applying this condition to Eq. (2.24) results in the following discretized form near the interface and boundary:

$$\left[\frac{\partial}{\partial x_3}\left(\frac{1}{\rho}\frac{\partial\hat{\Pi}}{\partial x_3}\right)\right]_{k+1/2} = \begin{cases} \dfrac{\frac{1}{\rho_{k+1}}\frac{\hat{\Pi}_{k+3/2}-\hat{\Pi}_{k+1/2}}{x_{3,k+3/2}-x_{3,k+1/2}}}{x_{3,k+1}-x_{3,k}}, & k=0,I, \\[4mm] \dfrac{-\frac{1}{\rho_k}\frac{\hat{\Pi}_{k+1/2}-\hat{\Pi}_{k-1/2}}{x_{3,k+1/2}-x_{3,k-1/2}}}{x_{3,k+1}-x_{3,k}}, & k=I-1,N_3-1. \end{cases} \tag{2.25}$$

We remark here that from Eq. (2.25), it is understood that ρ_I does not appear in the discretized Poisson equation of $\hat{\Pi}$. In other words, there is no need to specify the value of density at the interface. Substituting Eqs. (2.24) and (2.25) into Eq. (2.16) results in a tridiagonal linear equation system of $\hat{\Pi}$. Once $\hat{\Pi}$ is obtained, the velocity field is evolved to step $(n+1)$ based on Eq. (2.15).

Fig. 2 shows the flowchart of the proposed method. As shown in the figure, the new point of the proposed is the use of the effective viscosity at the interface. This allows us to derive a consistent equation of the intermediate velocity $\hat{v}_i$ in two fluid phases,

```
┌─────────────────────────────────────┐
│           Start simulation          │
└─────────────────────────────────────┘
                  │
┌─────────────────────────────────────┐
│ Calculate the interface effective    │
│ viscosity (Eq. (2.23))               │
└─────────────────────────────────────┘
                  │
┌─────────────────────────────────────┐
│ Calculate the coefficient of the     │
│ tridiagonal equation of v̂ᵢ (Eq. (2.20))│
└─────────────────────────────────────┘
                  │
┌─────────────────────────────────────┐
│ Calculate the right hand side of the │
│ equation of v̂ᵢ (Eqs. (2.17), (2.19),  │
│ and (2.20))                          │
└─────────────────────────────────────┘
                  │
┌─────────────────────────────────────┐
│ Solve Eq. (2.14) to obtain the       │
│ velocity v̂ᵢ at the intermediate step  │
└─────────────────────────────────────┘
                  │
┌─────────────────────────────────────┐
│ Solve Eq. (2.16) to obtain the       │
│ pseudo pressure field Π̂              │
└─────────────────────────────────────┘
                  │
┌─────────────────────────────────────┐
│ Update the velocity field to         │
│ a new step (Eq. (2.15))              │
└─────────────────────────────────────┘
                  │
          < Fully developed? >──── No ───┐
                  │ Yes                   │
┌─────────────────────────────────────┐  │
│         Calculate statistics        │  │
└─────────────────────────────────────┘  │
                  │                       │
        < Statistics converged? >── No ───┘
                  │ Yes
   / Output data of statistics and  /
   /     instantaneous field        /
                  │
┌─────────────────────────────────────┐
│          Finish simulation          │
└─────────────────────────────────────┘
```
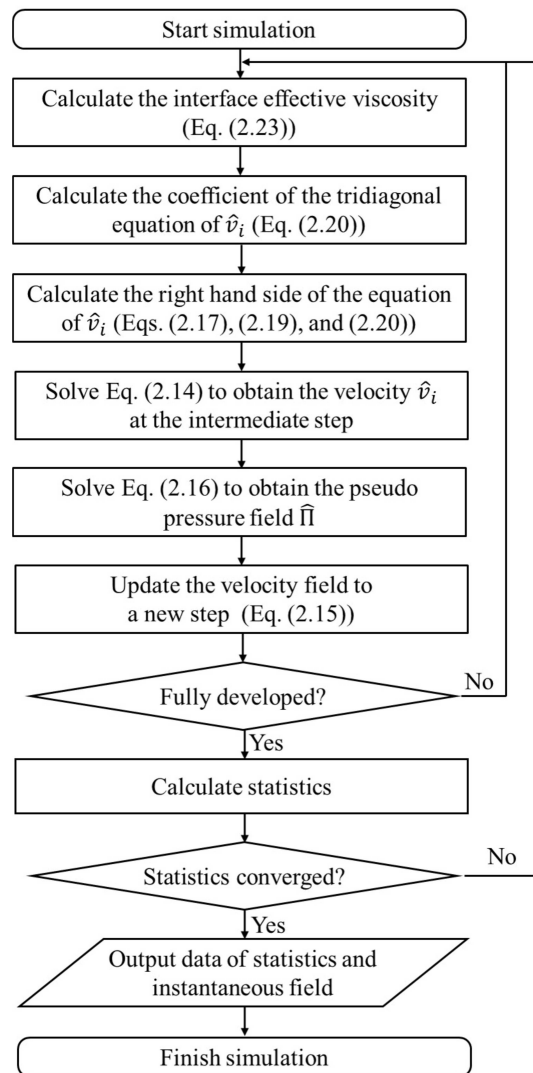
Figure 2: Flowchart of the code for direction numerical simulations of two-layer turbulent channel flows.

and the solution of this equation satisfies the interface conditions given by Eqs. (2.5) and (2.6). On the opposite, if the interface conditions are not strictly satisfied as in Lombardi *et al.* [13] and Liu *et al.* [14], the motions of two fluid phases are weekly coupled. It is shown in Section 3.2 that the week coupling approach results in an inaccurate prediction of the velocity field in the water. An alternative approach for achieving strong coupling in the simulation of the two-layer channel flow is to adopt an inner iteration. However, as noted by Yang and Shen [20], three to five inner iterations are usually needed at each step to satisfy the interface conditions, leading to the increase in the computational cost by three to five times. In summary, compared with the previous methods studying the same

problem, the proposed method is novel in both simulation accuracy and computational cost.

3 Results

3.1 Resolution test

The new method is tested using the case considered by Liu *et al.* [14]. The ratios of density and dynamic viscosity between water and air are set to $\rho_w/\rho_a = 828$ and $\mu_w/\mu_a = 65.1$, respectively. The flow is driven by the plate at the top of air, moving at a constant speed U. The computational domain size is $L_1 \times L_2 \times L_3 = 2\pi h \times \pi h \times 2h$. The Reynolds number is $Re = Uh/\nu_a = 9593$, where $\nu_a = \mu_a/\rho_a$ is the kinematic viscosity of air. In order to examine the effect of grid resolution on the simulation results, the simulations are conducted on three sets of grids. Table 1 summarizes the numbers of grid points and grid resolutions of different cases. In the table, Δ_1^+ and Δ_2^+ represent the grid resolution in the streamwise and spanwise directions, respectively, while $\min(\Delta_3^+)$ and $\max(\Delta_3^+)$ denote respectively the minimum and maximum grid resolution in the vertical direction. The superscript "$+$" denotes the quantities non-dimensionalized using u_τ and ν/u_τ as characteristic velocity and length scales, respectively, where $u_\tau = \sqrt{\tau_m/\rho}$ is the mean wall-friction velocity, with τ_m being the wall shear stress averaged over time and horizontal plane. Note that the values of τ_m on the water and air sides are identical due to the continuity of shear stress at the interface, but the values of both u_τ and ν/u_τ on the water and air sides are different because of the differences in the density ρ and dynamic viscosity μ. Therefore, two values are given for each grid resolution in Table 1, separated by the vertical line. The smaller one is the value on the water side, while the larger one is that on the air side. The ratio between the characteristic length scale on the water and air sides is $(\nu_w/u_{\tau,w}):(\nu_a/u_{\tau,a}) = 2.27$. As summarized in Table 1, the grid resolution is refined progressively from case 1 to case 3. The value of the frictional Reynolds number $Re_\tau = u_\tau h/\nu$ is also given in the table. From Table 1, it is seen that the value of Re_τ is 120 and 272 on the water and air sides, respectively, in both cases 2 and 3, indicating that the resolution independency is achieved in case 2. These two values of Re_τ are also close to those of Liu *et al.* [14] (120 and 271 on the water and air sides, respectively). In contrast, the values of $Re_{\tau a}$ and $Re_{\tau w}$ of case 1 (125 and 282 on the water and air sides, respectively) are larger than those of cases 2 and 3, indicating that the grid resolution of case 1 is insufficient to make an accurate prediction of turbulent statistics.

Table 1: Key parameters of simulation cases.

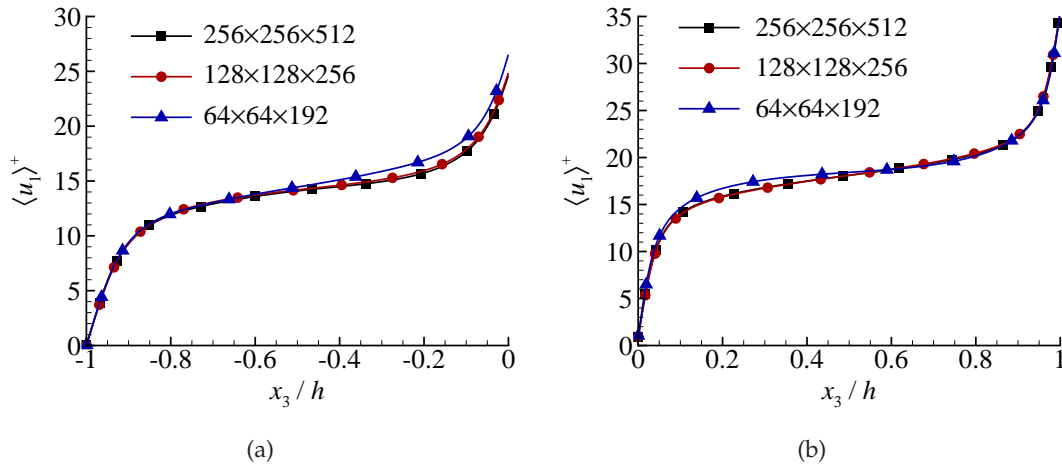| Case	$N_1 \times N_2 \times N_3$	Δ_1^+	Δ_2^+	$\min(\Delta_3^+)$	$\max(\Delta_3^+)$	Re_τ
1	$64 \times 192 \times 64$	11.8|26.7	5.92|13.4	0.05|0.11	3.11|7.02	125|282
2	$128 \times 256 \times 128$	5.92|13.4	2.96|6.68	0.04|0.08	2.33|5.27	120|272
3	$256 \times 512 \times 256$	2.96|6.68	1.48|3.34	0.02|0.04	1.16|2.63	120|272

Figure 3: Effect of grid resolution on the profiles of $\langle u_1 \rangle^+$ on the (a) water side and (b) air side.
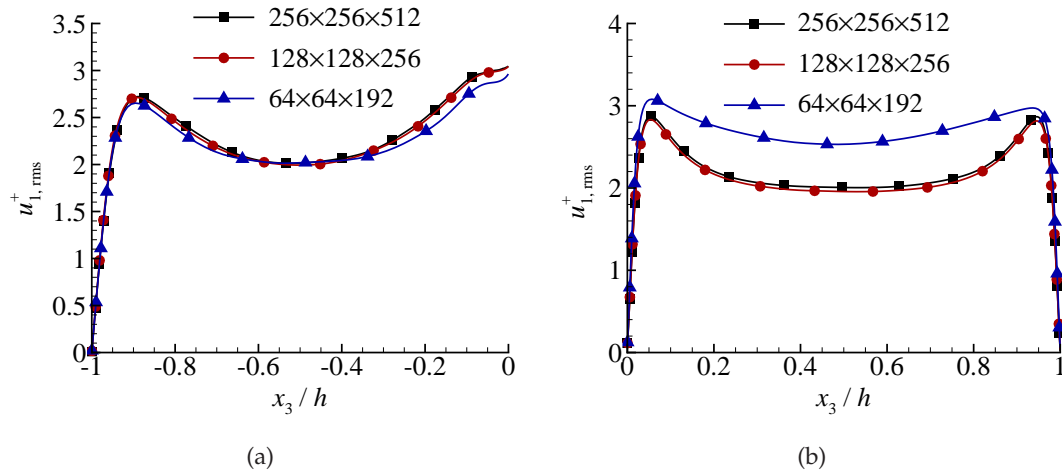

Figure 4: Effect of grid resolution on the profiles of $u_{1,\text{rms}}^+$ on the (a) water side and (b) air side obtained from the proposed method.

Figs. 3 and 4 compare the profiles of mean streamwise velocity $\langle u_1 \rangle^+$ and root-mean-square (RMS) velocity $u_{1,\text{rms}}^+ = \langle u_1' u_1' \rangle^{1/2}$ of different cases, respectively. To present the results, a pair of angular brackets $\langle \cdot \rangle$ are used to denote the averaging over time and horizontal plane; the difference between instantaneous velocity and mean velocity is defined as velocity fluctuation, denoted using a prime. As shown in Fig. 3, the mean velocity profiles of the three cases are close to each other on both the water and air sides. The RMS velocity $u_{1,\text{rms}}^+$ is more sensitive to the grid resolution than the mean velocity $\langle u_1 \rangle^+$. From Fig. 4, it is seen that the profiles of $u_{1,\text{rms}}^+$ of cases 2 and 3 also agree well with each other, indicating that the grid resolution of case 2 is sufficient to make an accurate prediction

of both mean streamwise velocity and RMS velocity. In contrast, the profiles of $u_{1,\mathrm{rms}}^+$ of case 1 deviates from those of cases 2 and 3, indicating that the grid resolution of case 1 is unsatisfactory for direct numerical simulations (DNS).

3.2 Comparison with results obtained from weak-coupling approach

To demonstrate the effect of the coupling approach on the turbulent statistics, we compare the results of case 2 (Table 1) based on the strong-coupling approach with those of Liu *et al.* obtained from the weak-coupling approach [14]. Fig. 5 compares the profiles of mean streamwise velocity $\langle u_1 \rangle^+$ based on strong- and weak-coupling approaches. As shown in Fig. 5(b), the profiles of $\langle u_1 \rangle^+$ based on strong- and weak-coupling approaches collapse on the air side. However, the discrepancy in $\langle u_1 \rangle^+$ between strong- and weak-coupling approaches is evident on the water side, particularly near the interface. The effect of the coupling approach on the RMS velocity is similar from Fig. 6, which compares the profiles of $u_{i,\mathrm{rms}}^+$ obtained from strong- and weak-coupling approaches. As shown, the differences in the results mainly exhibit in the profiles of $u_{1,\mathrm{rms}}^+$ on the water side, near the interface.

The observation that the coupling approach does not influence the results on the air side can be explained by the analogy between the two-fluid flows and the fluid-solid interaction problems. It is known from many numerical studies of fluid-solid interaction problems that if the density ratio between the solid body and fluid is much larger than unity, the results obtained from strong- and weak-coupling approaches are consistent [31, 32]. This situation is satisfied on the air side in the two-layer channel flow as the density ratio between water and air is $\rho_w/\rho_a = 828$. However, the water is different from a solid
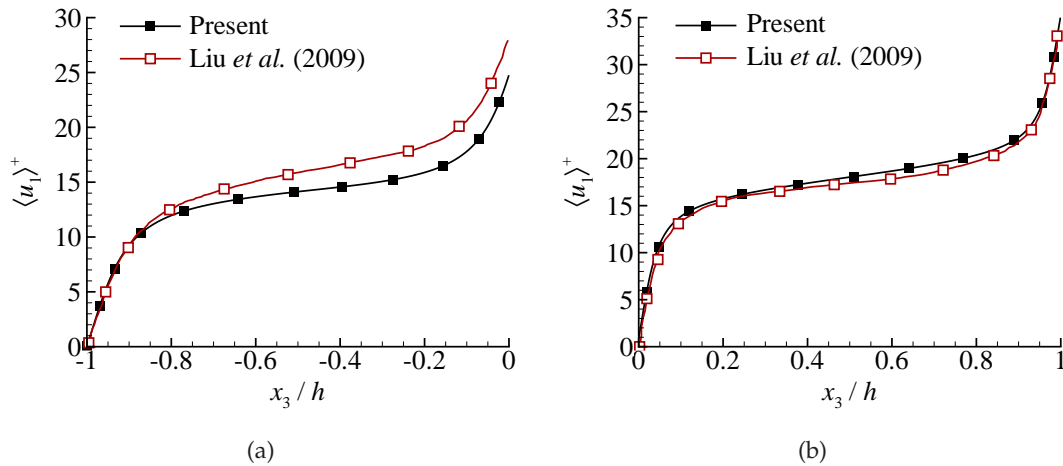

Figure 5: Profiles of $\langle u_1 \rangle^+$ on the (a) water side and (b) air side obtained from the proposed method. The results of Liu *et al.* [14] are superimposed for comparison.
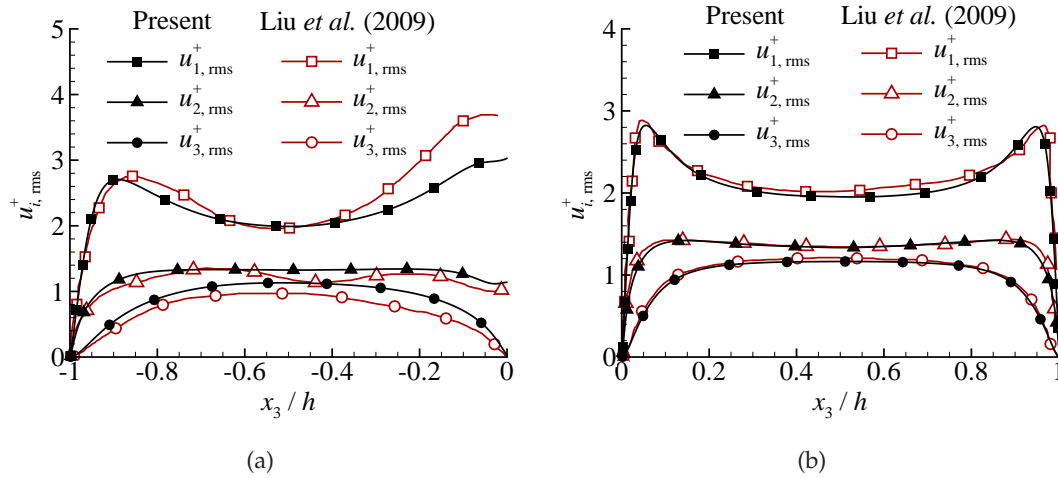
Figure 6: Profiles of $u_{i,\mathrm{rms}}^+$ on the (a) water side and (b) air side obtained from the proposed method. The results of Liu *et al.* [14] are superimposed for comparison.

body. In the flow-structure interactions, the motion of solid body is mainly driven by the normal stress of fluid exerted on the body surface, while in the two-layer channel flow, the motion of water is driven by the shear stress at the interface. The results shown in Figs. 5 and 6 indicate that the strong-coupling approach is necessary if the motion of water is of interest.

4 Conclusions

In the present research, a new strong-coupling method is proposed for numerical simulations of two-layer turbulent channel flows. The key of the proposed method is the implementation of an effective dynamic viscosity at the interface, defined as the harmonic averaging of the dynamic viscosities of two fluid phases. By adopting this effective dynamic viscosity, the motions of two fluid phases are strongly coupled in the simulation. As such, no inner iteration is needed, while the interface condition is satisfied automatically. Therefore, the use of the effective interface viscosity significantly reduces the computational cost and improves the simulation accuracy.

The proposed method is tested in the context of the direct numerical simulation of a two-layer turbulent Couette flow at a low Reynolds number. The turbulent statistics obtained from the proposed strong-coupling method are compared with the results of Liu *et al.* [14], who used a weak-coupling numerical method to simulate the same case. It is found that the profiles of mean velocity and RMS velocity on the water side obtained from the strong- and weak-coupling approaches are significantly different. This observation evidently shows the importance of applying the strong-coupling method for numerical simulations of two-layer turbulent channel flows.

Acknowledgments

References

[1] P. P. Sullivan, J. C. McWilliams, and C.-H. Moeng. Simulation of turbulent flow over idealized water waves. *Journal of Fluid Mechanics*, 404:47–85, 2000.

[2] D. Yang and L. Shen. Direct-simulation-based study of turbulent flow over various waving boundaries. *Journal of Fluid Mechanics*, 650:131–180, 2010.

[3] D. Yang and L. Shen. Direct numerical simulation of scalar transport in turbulent flows over progressive surface waves. *Journal of Fluid Mechanics*, 819:58–103, 2017.

[4] W.-Y. Zhang, W.-X. Huang, and C.-X. Xu. Very large-scale motions in turbulent flows over streamwise travelling wavy boundaries. *Physical Review Fluids*, 4:054601, 2019.

[5] V. Borue, S. A. Orszag, and I. Staroselsky. Interaction of surface waves with turbulence: Direct numerical simulations of turbulent open-channel flow. *Journal of Fluid Mechanics*, 286:1–23, 1995.

[6] D. T. Walker, R. I. Leighton, and L. O. Garza-Rios. Shear-free turbulence near a flat free surface. *Journal of Fluid Mechanics*, 320:19–51, 1996.

[7] L. Shen, X. Zhang, D. K. P. Yue, and G. S. Triantafyllou. The surface layer of free-surface turbulent flows. *Journal of Fluid Mechanics*, 386:167–212, 1999.

[8] B.-Q. Deng, Z. Yang, A. Xuan, and L. Shen. Influence of Langmuir circulations on turbulence in the bottom boundary layer of shallow water. *Journal of Fluid Mechanics*, 861:275–308, 2019.

[9] A. Xuan, B.-Q. Deng, and L. Shen. Study of wave effect on vorticity in Langmuir turbulence using wave-phase-resolved LES. *Journal of Fluid Mechanics*, 875:173–224, 2019.

[10] R. Scardovelli and S. Zaleski. Direct numerical simulation of free-surface and interfacial flow. *Annual Review of Fluid Mechanics*, 31:567–603, 1999.

[11] B.-Q. Deng, Y. Hu, X. Guo, R. A. Dalrymple, and L. Shen. Numerical study on the dissipation of water waves over a viscous fluid-mud layer. *Computers and Fluids*, 158:107–119, 2017.

[12] Z. Yang, B.-Q. Deng, and L. Shen. Direct numerical simulation of wind turbulence over breaking waves. *Journal of Fluid Mechanics*, 850:120–155, 2018.

[13] P. Lombardi, V. DeAngelis, and S. Banerjee. Direct numerical simulation of near-interface turbulence in coupled gas-liquid flow. *Physics of Fluids*, 8:1643–1665, 1996.

[14] S. Liu, A. Kermani, L. Shen, and D. K. P. Yue. Investigation of coupled air–water turbulent boundary layers using direct numerical simulations. *Physics of Fluids*, 21:062108, 2009.

[15] J. Kim, P. Moin, and R. Moser. Turbulence statistics in fully developed channel flow at low Reynolds number. *Journal of Fluid Mechanics*, 177:133–166, 1987.

[16] X. Liu, F. Song, and C. Xu. An efficient spectral method for the inextensible immersed interface in incompressible flows. *Communication in Computational Physics*, 25:1071–1096, 2019.

[17] B. E. Treeby, E. S. Wise, and B. T. Cox. Nonstandard Fourier pseudospectral time domain (PSTD) schemes for partial differential equations . *Communication in Computational Physics*, 24:623–634, 2018.

[18] Z.-X. Li, J. Lao, and Z.-Q. Wang. Pseudospectral methods for computing the multiple solutions of the Schrödinger equations. *Communication in Computational Physics*, 23:822–845, 2018.

[19] P. Song, T. Yang, Y. Ji, Z. Wang, Z. Yang, L. Chen, and L. Chen. A comparison of Fourier spectral iterative perturbation method and finite element method in solving phase-field equilibrium equations. *Communication in Computational Physics*, 21:1325–1349, 2017.

[20] D. Yang and L. Shen. Simulation of viscous flows with undulatory boundaries. Part II: Coupling with other solvers for two-fluid computations. *Journal of Computational Physics*, 230:5510–5531, 2011.

[21] D. Yang and L. Shen. Simulation of viscous flows with undulatory boundaries: Part I. Basic solver. *Journal of Computational Physics*, 230:5488–5509, 2011.

[22] A. Xuan and L. Shen. A conservative scheme for simulation of free-surface turbulent and wave flows. *Journal of Computational Physics*, 378:18–43, 2019.

[23] J. Kim and P. Moin. Application of a fractional-step method to incompressible navier-stokes equation. *Journal of Computational Physics*, 59:308–323, 1985.

[24] L. Fang, L. Shao, J.-P. Bertoglio, G. X. Cui, C.-X. Xu, and Z. Zhang. An improved velocity increment model based on Kolmogorov equation of filtered velocity. *Physics of Fluids*, 21:065108, 2009.

[25] B.-Q. Deng and C.-X. Xu. Influence of active control on STG-based generation of streamwise vortices in near-wall turbulence. *Journal of Fluid Mechanics*, 710:234–259, 2012.

[26] B.-Q. Deng, C.-X. Xu, W.-X. Huang, and G.-X. Cui. Strengthened opposition control for skin-friction reduction in wall-bounded turbulent flows. *Journal of Turbulence*, 15(2):122–143, 2014.

[27] B.-Q. Deng, W.-X. Huang, and C.-X. Xu. Origin of effectiveness degradation in active drag reduction control of turbulent channel flow at $Re_\tau = 1000$. *Journal of Turbulence*, 17:758–786, 2016.

[28] M. Ge, D. Tian, and L. Yongqian. Dynamic evolution process of turbulent channel flow after opposition control. *Fluid Dyn. Res.*, 49:015505, 2017.

[29] M.-W. Ge, L. Fang, and Y.-Q. Liu. Drag reduction of wall bounded incompressible turbulent flow based on active dimples/pimples. *Journal of Hydrodynamics*, 29:261–271, 2017.

[30] F. Liu, L. P. Lu, and L. Fang. Non-equilibrium turbulent phenomena in transitional channel flows. *Journal of Turbulence*, 19:731–753, 2018.

[31] F. Sotiropoulos and X. Yang. Immersed boundary methods for simulating fluid-structure interaction. *Prog. Aerosp. Sci.*, 65:1–21, 2014.

[32] J. Yang and F. Stern. A non-iterative direct forcing immersed boundary method for strongly-coupled fluid-solid interactions. *Journal of Computational Physics*, 295:779–804, 2015.